CHAPTER 1

INTRODUCTION

1.1 FROM ELECTRONICS TO OPTOELECTRONICS

The huge success of semiconductor electronics came from the fact that semiconductors can have a miniscule size and can dynamically change their conduction properties, leading to an elegant successor of the previously used vacuum tubes.

After the first demonstration of the dynamically tunable conductance of a germanium based transistor by J. Bardeen and W. Brattain in the group of W. Shockley in Bell Laboratories, there was a huge effort on the growth, miniaturization, and improvement of the modulation speed of semiconductor based devices. The use of silicon was widely spread and is nowadays the main material used in most electronic components. Computer processing units (CPUs) are one of the most notable examples of the use of silicon, where the modulation speed has now reached its physical limits. The physically induced limits on the bandwidth of the modulation of electronic signals presents serious limitations on the amount of information transferred and processed and, thus, new technologies needed to be found.

Using optical signals presents serious advantages and the idea of combining optics with electronics gave birth to a new category of devices: optoelectronics. However, creating, capturing, and modulating optical signals is complicated, especially when done with silicon which is an indirect bandgap material. The use of direct bandgap semiconductors was the key to this problem, which established III-V compounds in optoelectronics. The subsequent improvement of the growth techniques and quality allowed for the development of complicated structures, with the most remarkable being the semiconductor laser, dating back to the 1960s [1]. Many years later, lasing from a Vertical Cavity Surface Emitting Laser (VCSEL) was demonstrated [2]. The motivation behind VCSELs was to lower the lasing threshold and to force single mode emission which led to the creation of microcavity structures characterized by the weak coupling regime.

The increasing quality of the materials and the narrowing linewidths allowed for the crossover from the weak to strong coupling regime. The first demonstration of strong coupling in a planar microcavity was done for the first time by C. Weisbuch [3]. The new eigenstates that occur in this type of structure are occupied by bosonic quasi particles with extremely low mass.

They were first conceived for bulk volumes by Hoppfield [4] in 1958 who considered the coupling of propagating photons with matter excitations.

Microcavities in the strong coupling regime are inherently interesting systems: not only are they a textbook example of light-matter interactions and normal mode splitting, but the quasiparticles (exciton-polaritons) that are formed in this type of structures have an interesting dispersion in the form of a trap in momentum space and an extremely low mass on the order 1/100,000 (10^{-5}) the free electron mass.

The ease of the addressability of this type of dispersion, the polarization properties, the inherent possibility of non-linear scattering processes, and the bosonic nature of the polaritons has made these systems an extremely agile and alluring subject of study with numerous applications and rich fundamental physics.

1.2 FROM LOUIS DE BROGLIE TO CONDENSATION OF DILUTE ATOMIC GASES

It was in 1924 that Louis de Broglie proposed in his Ph.D. thesis [5] the concept of the wave nature of particles stating that each particle has a wave associated to it. One year later, Einstein, who had fully endorsed the wave particle duality, came across the work of Bose on the statistics for photons [6] and it was then that he realized that dilute atomic gases (matter) are expected to undergo a phase transition to a condensed state [7] with the lowest possible energy if their interatomic distances become comparable to the thermal de Broglie wavelength.

This idea became widely accepted by the scientific community only after the first observation of superfluidity by Kapitsa [8] in 1938, after which London had intuitively done the connection of superfluidity with the phenomenon of condensation described by Einstein [9].

Lots of efforts to create a consistent theory to describe superfluidity and condensation were made, in the course of which, quantized vortices were first predicted by Onsager [10], then later revisited by Feynman [11], and experimentally observed for the first time in 1960 by Hall and Vinen [12].

In 1975 Volovik and Mineev [13] and a few months later Cross and Brinkman [14], taking into account the spinor nature for superfluids, predicted a new type of excitation, the half quantum vortex.

Condensation of dilute atomic gases was first reported in 1995 when the groups of Ketterle [15] and Cornell [16], using a combination of cooling techniques that were developed previously, succeeded in getting the right conditions for the observation of condensation using sodium and rubidium atoms respectively.

In 1996, the long predicted half quantum vortices are reported for the first time by Kirtley [17] in high temperature superconductors. In the following years, a huge amount of work has been done on condensates of dilute atomic gases of various species for both theory and experiment and a deep understanding of the properties of equilibrium condensates is achieved.

1.3 CONDENSATION AND OPTOELECTRONICS: A DREAM BECOMES REALITY

The phenomenon of condensation has not only resided in the atomic or superfluid helium community but it has rather stimulated the semiconductor community from the early years. As early as 1962, excitons were proposed by Blatt and Moskalenko as promising candidates for the demonstration of Bose-Einstein condensation [18]. The bosonic nature of these quasiparticles – that are made of electrons and holes held together by the coulomb interaction – and their light mass, were the main reasons for the long but fruitless efforts to demonstrate condensation.

After the demonstration of strong coupling in semiconductor microcavities [3] and the creation of polaritons that are composite bosons with a half exciton-half photon nature, a new wave of excitement rushed through the solid state community. The polariton dispersion could act as a trap in momentum space and the mass of polaritons was four orders of magnitude lighter than that of excitons, theoretically allowing condensation even at room temperature.

Polariton non-equilibrium condensation was proposed first by Imamoglu et al. [19]. Several indications of the bosonic nature were found in pioneering experiments by the group of Baumberg, Scolnick and Deveaud. The weak exciton binding energy of the first generation samples did not allow observation of macroscopic occupations of the lower bottom polariton branch, as the systems lost the strong coupling.

The breakthrough came by the samples of R. André which were based on II-VI compounds (CdTe, CdMnTe, CdMgTe) where, because of the higher exciton binding energies, convincing indications of macroscopic occupation in the strong coupling regime were reported. The pioneering work of Richard et al. [20] although truly outstanding, it lacked experimental evidence of macroscopic phase coherence (long range order) and therefore did not eliminate all ambiguity.

The first comprehensive and irrefutable evidence for condensation of exciton polaritons was reported in 2006 by the work of Kasprzak and Richard et al. [21]. This observation triggered a massive wave of excitement and immediately afterwards, condensation of exciton polaritons was reported for GaAs microcavities under stress [22] and, more recently, for planar GaAs

microcavities under non-resonant pumping [23]. Large efforts have been also devoted to get the same effects at room temperature and already solid indications are reported using large bandgap materials like GaN [24] and, more recently, ZnO materials [25].

1.4 OVERVIEW

The object of this book is to reveal fundamental properties of exciton polariton condensates in CdTe microcavities. After the demonstration of condensation of microcavity polaritons by Kasprzak *et al.* in 2006, many questions needed to be answered. Triggered by these questions, the experimental investigations that were pursued in the years to come revealed many fundamental aspects of polariton condensates. In addition, intense interactions with different theoretical groups has proved very fruitful as most of the observed phenomena were better understood after the reproduction of the observed phenomenology by theory.

The main characteristic of polariton condensates in CdTe microcavities is that condensation takes place in the existent disorder of the sample acquired during epitaxial growth. Disorder is thus expected to play a major role on the behavior of the condensates depending on its characteristics. In addition, the short lifetime of the polaritons renders polariton condensates out of equilibrium, because the steady state is a balance between losses (outgoing flows) and pumping from the excitonic reservoir (incoming flows).

The complex interplay of both the disorder and the non-equilibrium character has given rise to a very rich phenomenology.

Chapter 2 gives a brief account of the basics of microcavity polaritons and polariton condensates and Chapter 3 is dedicated to the sample and the methods used during this work.

Chapters 4 and 5 investigate the spectral properties of polariton condensates and their connection with the observation of long range spatial coherence. They show the diversity that one can find in polariton condensates as a function of the disorder and the reservoir dynamics.

Chapters 6 and 8 are a series of experiments on the observation of quantized conventional vortices and their behavior in CW and time resolved experiments showing that disorder and non-equilibrium can lead to the creation and pinning of vortices without the need to stir the condensates.

Chapter 7 deals with a new type of vortex in polariton condensates when under specific circumstances the spinor nature of the condensates comes into play and the conventional full vortices are too costly to form. It is an account on the observation of the celebrated case of half quantum vortices.

Finally Chapter 9 is dedicated to the temporally and spectrally resolved studies of a polaritonic Josephson junction where evidence of oscillating currents is provided by density and phase studies.

CHAPTER 2

CONDENSATION AND EXCITON-POLARITONS

Bose-Einstein Condensates are often considered as the fifth state of matter. There is an enormous beauty in their physics and there is a lot to be learned from them, as they are the ideal systems to observe quantum phenomena in a macroscopic level. Atomic condensates have attracted a huge interest after their first observation in 1995 by Cornell [15] and Ketterle [16] and, although they are extremely difficult to achieve, many groups worldwide carry out fundamental research on them. The main difficulty that is inherent to atomic condensates is the extremely low temperatures that are needed (on the order of nanokelvin) because of the large mass of atoms. Things would be much simpler if the condensing bosonic particles where less heavy. Along this line, solid state systems have been proposed as candidates for condensation and extended efforts have been done for the demonstration of condensation of magnons [26], excitons [27] and more recently polaritons [21]-[25]. In this chapter, the basics of condensation will be presented along with the basics of microcavity polaritons.

2.1 BOSONS AND CONDENSATION

The phenomenon of condensation of bosonic particles is based on the particular property of bosons to be indistinguishable. The mere bosonic nature forces the bosonic creation and annihilation operators to obey the so called bosonic commutation relations. Using as a starting point these commutation relations, it can be shown that scattering to a state with N particles is done at a rate of N+1. This stimulation of scattering is an effect purely related to the bosonic nature of particles and is often called the bosonic stimulation which is a key feature for the condensation.

In the early 1920's, after the observation of the photoelectric effect and its explanation by Einstein suggesting that light should behave as discrete packets or quanta (photons) [28], it was commonly accepted that light has a dual nature and behaves as waves or particles according to the circumstances. In 1924, following the reasoning that there is symmetry in nature, Luis de Broglie proposed that similarly to photons, matter particles should also have

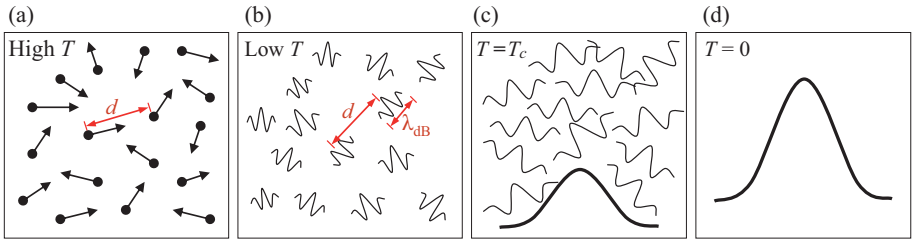

Figure 2.1 (a) Depiction of the particles of a gas at high temperature: the particles behave like billiard balls and the interatomic distances are huge with respect to particle size. (b) A gas of particles at low temperature where the de Broglie wavelength is non-negligible and the particles can be described as wavepackets. (c) The particles at critical temperature for condensation: large overlap of the wavefunction and creation of a macroscopic wave. (d) For $T = 0$, all particles are part of the condensate that behaves like a giant matter wave.

a dual nature and, therefore, suggested that particles should have a wave associated to them [5]. The wavelength of this wave is directly related to the particle momentum, i.e., $\lambda_{dB} = h/p$. When considering gases, from the Maxwell-Boltzmann distribution it can be shown that a typical particle momentum is on the order of $(2mK_BT)^{1/2}$, corresponding to the peak of the distribution and, therefore, the de Broglie wavelength of a particle in a gas is given by

$$\lambda_{dB} = \sqrt{\frac{2\pi\hbar^2}{mK_BT}} \tag{2.1}$$

and it is inversely proportional to both the mass and temperature. In a gas with temperature T, the atoms behave like billiard balls where they traverse large distances until they elastically collide with one another to change their direction. In this picture, the indistinguishability of the atoms does not apply. When the temperature of the particles is low enough (below a critical value T_c), the thermal de Broglie wavelength becomes comparable to the interatomic distances. Then the wavepackets of the particles begin to overlap and, under this particular condition, the indistinguishability comes into play. Consequently, below the critical temperature, bosonic particles undergo a transition towards a phase where all the particles massively occupy a single quantum state, forming a condensate.

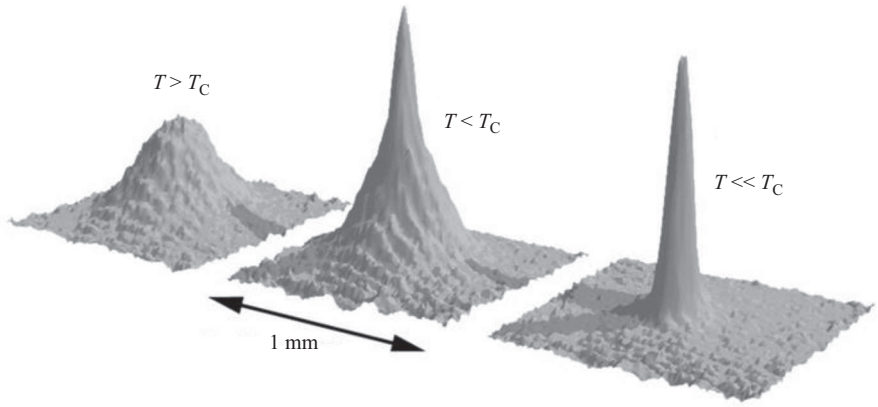

Figure 2.2 Distribution of atoms after an atomic cloud has been released and allowed to expand for different temperatures. For high temperatures ($T > T_C$), the final distribution is very broad demonstrating the high momenta of the atoms. When the atom cloud is close to the critical temperature ($T < T_C$), a peak can be resolved corresponding to a large fraction of very low velocity atoms of the condensate. Far below the critical temperature ($T << T_C$), all atoms are condensed and, therefore, will not expand as they have minimal kinetic energy [29].

The condensate state is then characterized by the establishment of macroscopic phase coherence and the particles in the condensed state are described by a single wavefunction. The relation that connects the atomic density at which condensation occurs with the de Broglie wavelength is $n\lambda_{dB}^3 \approx 2.616$ [30] from which one can calculate the critical temperature for condensation to be:

$$T_c = \frac{2\pi\hbar^2}{m}\left(\frac{n}{2.612}\right)^{2/3} \tag{2.2}$$

From this relation, it is straight forward to see that to attain higher critical condensation temperatures it is necessary either to reduce the bosonic particle mass or to increase their density.

2.2 MICROCAVITIES

From Equation 2.2, it is clear that the mass of the particles participating in the condensation transition should be as low as possible to obtain higher critical condensation temperatures. In the solid state, and in particular in semiconductor structures, the bosonic nature of the material excitations (excitons) and their very low mass has led to extensive efforts for the demonstration

of Bose-Einstein condensation. Nevertheless although there are promising reports of condensation effects, no unambiguous demonstration is available yet. Coupling of matter excitons with light can, under specific circumstances (strong coupling), lead to the creation of new quasi-particles (new eigenstates) which are a coherent superposition of light (photons) and matter (excitons), the so called polaritons. Due to their photonic content, these particles are many orders of magnitude lighter than atoms or excitons and, thus, with their mass being $10^{-5}m_e$, have a critical temperature for condensation close to room temperature. The main concepts of polaritons are briefly described later on.

2.2.1 DBR cavities and the transfer matrix method

A key feature for the development of systems where excitons and photons are strongly interacting is to be able to confine both excitons and photons to a small volume for extended periods of time. This confinement ensures that the interaction of the photons with the excitons occurs in an effective way.

The use of Fabry-Perrot resonators is ideal for photon trapping over prolonged periods of time given that the reflectivity of the mirrors is high enough. The confinement along the z direction (along the cavity spacer) forces the wavevector along z to have discrete values of $k_z L_c = N\pi$ where L_c is the spacer length. The total wavevector of the trapped photons, $k_o = n_c \cdot \omega/c$, decomposes to $k_o^2 = k_z^2 + k_{xy}^2$ from where one can retrieve by Taylor expansion the parabolic photon dispersion:

$$E_c\left(k_{xy}\right); \frac{\hbar c}{n_c} k_z + \frac{1}{2}\frac{\hbar c}{n_c}\frac{k_{xy}^2}{k_z} \tag{2.3}$$

The lifetime of a cavity photon is directly related to the reflectivity of the mirrors. It can be shown that

$$\frac{1}{\tau_c} \propto \frac{1-R}{\sqrt{R}}$$

where τ_c is the photon lifetime. For the efficient confinement of light, the use of metallic mirrors is restrictive, because of the low reflectivity. The solution to this problem is the growth of distributed Bragg reflectors where alternating layers with high and low refractive index are grown to give rise to the appearance of stopbands to the photonic mode (very high reflectivity zones).

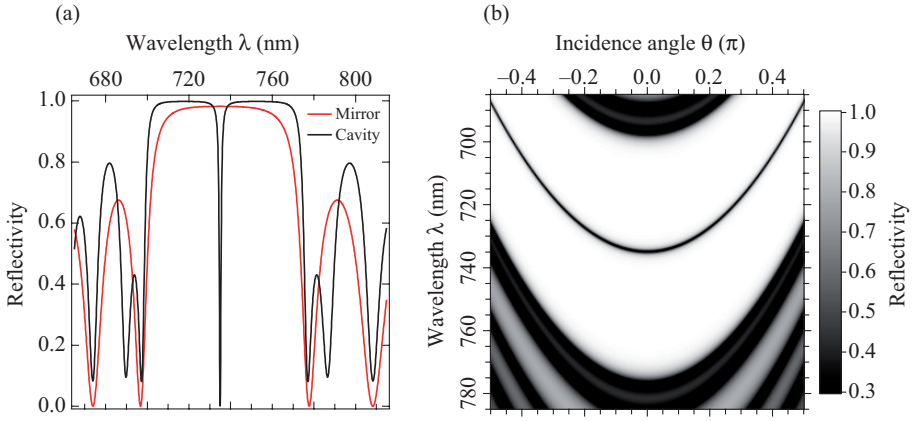

Figure 2.3 Transfer matrix method reflectivity calculations. (a) Reflectivity spectra of a single mirror with 24 alternating layers of high (2.82) and low (2.52) refractive indices in red centered at 735 nm. In black is the reflectivity of a DBR cavity with 16 pairs for the front mirror, 24 pairs for the back mirror, and a 2λ spacer incorporated in between, tuned also at 735 nm. (b) Reflectivity spectra of the cavity as in (a), but for all possible incidence angles. The reflectivity profile at θ=0 corresponds to the one shown in panel (a). The stopband angle dependence is clearly visible on which the parabolic behavior of the optical mode is easily distinguishable (thin black line on broad white band).

The thickness of the alternating layers is λ/4 with λ being the so called Bragg wavelength that corresponds to the center of the high reflectivity region. The width of the stopband region is given by:

$$\Delta\lambda_{\text{stopband}} = \frac{2\lambda\Delta n}{\pi n_{\text{eff}}} \tag{2.4}$$

where Δn is the refractive index difference and n_{eff} is the effective refractive index given either by a mean value of the two refractive indices, if Δn is small, or by the geometric mean, if Δn is large. Using this kind of structure, it is possible to get reflectivities on the order of $R=0.999$ and which consequently increases dramatically the photon lifetimes. A very powerful method to simulate this kind of structure is the so called transfer matrix method (TMM). A detailed analysis on the calculation of the reflectivity spectra can be found in the literature [31].

In Figure 2.3(a), the reflectivity spectra of a single mirror with 32 pairs of high (2.82) and low (2.52) refractive indices is shown in red, calculated by the TMM. Superposed to it is the reflectivity of a DBR cavity (in black) with 16 pairs for the front mirror, 24 pairs for the back mirror, and a 2λ spacer incorporated in between. The refractive indices were chosen so as to represent

the indices of the compounds used in the actual microcavity (Sect. 3.1 and [32]) and the TMM was performed here for normal incidence. The reflectivity spectrum shows a strong dependence on the incidence angle which is expected from the behavior of the cavity photon parabolic dispersion. The TMM also allows for angle dependent reflectivity calculations and so the full simulation of the previous microcavity structure was performed for a range of incidence angles from $-\pi/2$ to $+\pi/2$. Figure 2.3(b) shows the reflectivity spectra of the cavity as in (a), but now for the full incidence angles. The reflectivity profile at $\theta=0$ corresponds to the one shown in panel (a). The expected parabolic dispersion (Eq. 2.3) is clearly visible on the resonant dip centered at the high reflectivity stopband (white wide band).

2.2.2 Excitons in quantum wells

For the efficient coupling of light with matter-excitations, it is necessary to trap light and force it to interact with an active medium. Trapping of light was presented in the previous section. The active medium in microcavities where matter-excitations can be generated is the semiconductor material itself which, when absorbing light, can form excitons. Excitons are electron-hole pairs bound together by the coulomb attractive interaction. As for the hydrogen atom case, the binding energy of excitons depends on their mass and the Bohr radius. Excitons created in quantum wells have much higher binding energies with respect to the unconfined case. In particular, their binding energy increases by a factor of 4 due to the confinement [33]. Thus, quantum well excitons are much more robust than bulk excitons. Their energy is described by:

$$E_x\left(k\right) = E_x\left(0\right) + \frac{\hbar^2 \cdot k_{//}^2}{2 \cdot M} \tag{2.5}$$

with M being the mass of the exciton and:

$$E_x\left(0\right) = E_{\mathrm{bg}} + E_{\mathrm{Q}} - \frac{\hbar^2}{2 \cdot m_r \cdot a_B^2} \cdot \frac{1}{\left(n - \frac{1}{2}\right)^2} \tag{2.6}$$

where the first two terms are the bandgap energy, E_{bg}, and the quantization energy (due to confinement) E_{Q}. The third term is the binding energy, which is a result of the coulomb interaction in the quantum well, m_{r} is the reduced mass, and α_{B} the Bohr radius. A measure of the optical activity of excitons (the probability that an absorbed photon will give an exciton) is the oscillator strength. It can be shown that the oscillator strength for confined excitons is

increased by a factor of 8 with respect to the unconfined case. The robustness of excitons in quantum wells and their increased optical activity are the key features that established the embedding of quantum wells in microcavities.

As excitons are composite particles occurring from the coulomb interaction of an electron with a hole, their spin depends on the spin of the two constituents. The spin of the conduction band electrons and the valence band holes, furthermore, depends on the crystal structure. CdTe, as well as GaAs, are Zinc-blend crystals and, thus, the structure of their energy bands is similar [34]. The precise band structure of this type of crystal can be calculated using the $k \times p$ method [35]. The lowest conduction band is an s orbital ($l=0$, $m_l=0$, $s=1/2$, $m_s=\pm 1/2$) which is two-fold degenerate. The uppermost valence band, on the contrary, is a p orbital which, in the absence of spin orbit coupling, is a six-fold degenerate state ($l=1$, $m_l=0, \pm 1$, $s=1/2$, $m_s=\pm 1/2$).

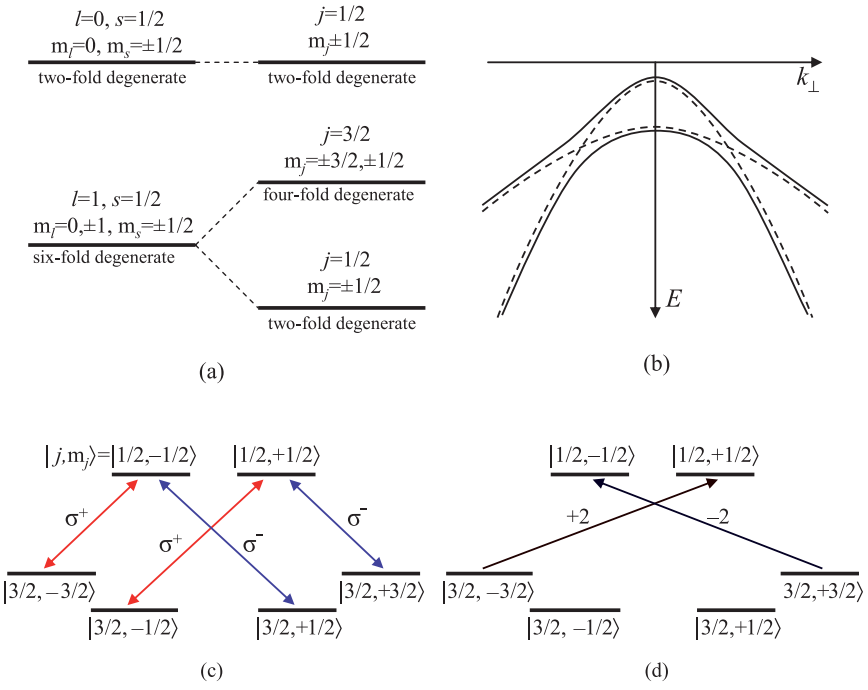

Figure 2.4 (a) Lowest conduction band and highest valence band at $k=0$ before (left) and after (right) spin-orbit coupling. (b) Heavy hole and light hole crossed bands in the absence (dashed lines) and presence (solid lines) of band mixing, because of the quantum confinement. The mixing leads to anti-crossing of the two bands. (c) Optical transitions that obey angular momentum conservation between the spin of excitons and the photon. In blue are the transitions that involve σ^- photons and in red are the transitions that involve σ^+ photons. (d) Dark exciton transitions that have a total spin of ± 2. These excitons have a very long lifetime, because they are optically inactive, but their presence contributes strongly to the interactions between the excitonic reservoir and polaritons.

Introducing spin-orbit coupling results in a lift of the degeneracy of the six-fold degenerate state for the creation of two new eigenstates with total angular momentum $j = l+s$ and projections $m_j = 0,\pm1/2, \pm1,\ldots, \pm j$ [36]. The initial and new eigenstates after spin-orbit coupling for $k = 0$, are shown in Figure 2.4(a). The $j = 3/2$ with $m_j = \pm3/2$ eigenstate is the so called heavy hole band and is degenerate with $j = 3/2$, $m_j = \pm1/2$ which is the light hole band. The $j = 1/2$, $m_j = \pm1/2$ is the so called spin-orbit split-off valence band.

Up to here, the description does not include any confinement and, hence, it is applicable only for the bulk conduction and valence bands. The effect of the quantum well confinement further modifies the band structure, as was demonstrated by Luttinger [35],[36]. Confinement leads to a crossing of the light hole band by the heavy hole band, as shown in Figure 2.4(b) with the dashed lines. In the framework of Luttinger, significant band mixing takes places and the two bands present anti-crossing, as seen in Figure 2.4(b) (solid lines).

In the direction of confinement, the otherwise heavy hole excitons are now lighter and the light hole excitons become heavier. This phenomenon is known as the "mass reversal" [35],[36]. Optical transitions can only take place if the total angular momentum of the created exciton coincides with the spin of the emitted/absorbed photon. More specifically, the spin of a photon, m_p, has to obey the equality $m_p = m_{je}-m_{jh}$. The excitons with total angular momentum ±2 are optically inactive, but can abundantly be created in non-resonant excitation experiments. The effect of their presence has, nevertheless, a non-negligible contribution in the exciton-polariton interactions. A large amount of work has been done on the spin of excitons, either for bulk semiconductors or quantum wells and the reader can find more in the cited works [35]-[38] and references therein.

2.3 POLARITONS

Microcavities were first created based on the concept of Vertical Cavity Surface Emitting Lasers (VCSELS) which are planar microresonators [2] with embedded quantum wells. These particular structures have relatively poor reflectivities, thus functioning in the weak coupling regime where the emission of a photon by an exciton is irreversible. The existence of the cavity modifies the photon field and actually acts as an enhancer of spontaneous emission in the cavity mode, an effect predicted by Purcell in 1946 [39]. The probability to find the exciton in the excited state is $P_{ex}(t) = -\exp(\gamma_c t)$ which drops exponentially with time at a rate given by the linewidth of the cavity mode γ_c.

An increased quality of the optical resonator though, dramatically changes the behavior. It can lead to sustained trapping of the emitted photon and, thus,

the probability that the exciton reabsorbs this photon becomes significant. For this case, the emission of a photon by the exciton becomes reversible and the system can undergo several energy exchanges before it dissipates. The probability to find an exciton is

$$P_{\text{ex}}(t) = \sum_n p(n) \cos^2\left(\frac{1}{2}\Omega_{\text{ef}}\sqrt{n+1}\ t\right)$$

with $p(n)$ being the probability to have n photons in the cavity and Ω_{ef} the Rabi frequency which describes the coupling strength between the exciton and photon [40].

2.3.1 Strong coupling

The energy exchange between excitons and photons in a high quality microcavity with embedded quantum wells, leads to the creation of new eigenstates that are coherent superpositions of the two initial states. The energy separation between the two new eigenstates is related to the coupling energy between the cavity photons and quantum well excitons. The Hamiltonian of the unperturbed system reads:

$$H_o = \sum_k E_x(k) \cdot b_k^\dagger b_k + \sum_k E_c(k) \cdot a_k^\dagger a_k \tag{2.7}$$

with the energy terms being the dispersions of excitons and photons as discussed in Sections 2.2.1 and 2.2.2. The interaction Hamiltonian reads:

$$H_{xc} = \sum_k \hbar\Omega \cdot \left(a_k^\dagger b_k + b_k^\dagger a_k\right) \tag{2.8}$$

where $\hbar\Omega$ is the interaction strength. The diagonalization of the total Hamiltonian will give the eigenenergies of the new eigenstates which, in matrix form, corresponds to the eigenvalues of the matrix:

$$M(k) = \begin{bmatrix} E_x(k) & \hbar\Omega \\ \hbar\Omega & E_c(k) \end{bmatrix} \tag{2.9}$$

The eigenvalues are:

$$\lambda_1 = E_U(k) = \frac{E_x(k) + E_c(k)}{2} + \frac{1}{2} \cdot \sqrt{\left(E_c(k) - E_x(k)\right)^2 + 4\hbar^2\Omega^2} \tag{2.10}$$

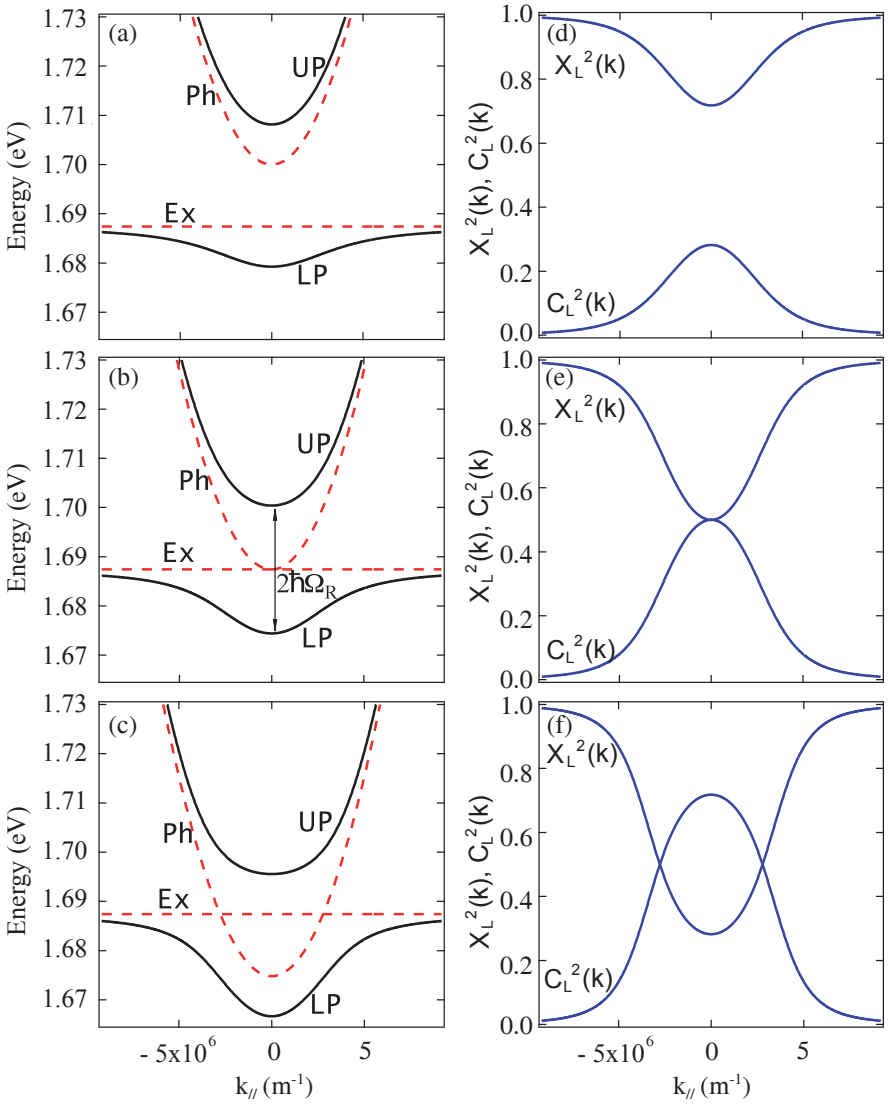

Figure 2.5 (a), (b), and (c) Upper and lower polariton dispersions in solid black lines along with the uncoupled exciton and photon dispersions (red dashed lines) for δ = +13 meV, 0 meV and –13 meV, respectively. The curvature of the excitonic dispersion (Ex) is negligible with respect to that of the photons (Ph). The splitting between the upper (UP) and lower polaritons (LP) is related to the Rabi frequency adjusted by the detuning. Here a splitting of 26 meV for zero detuning was used. (d), (e), and (f) Hopfield coefficients indicating the photonic and excitonic part of polaritons for three exciton-photon detunings: δ = +13 meV, 0 meV, and –13 meV, respectively. At $k_{//} = 0$ and zero detuning, lower polaritons are half photonic – half excitonic quasiparticles. Positive detuning makes lower polaritons more exciton-like whereas negative detuning make polaritons more photon-like.

and

$$\lambda_2 = E_L(k) = \frac{E_x(k) + E_c(k)}{2} - \frac{1}{2} \cdot \sqrt{\left(E_c(k) - E_x(k)\right)^2 + 4\hbar^2\Omega^2} \qquad (2.11)$$

which correspond to the so called upper and lower polariton energies. The difference, $\delta = (E_c(k) - E_x(k))$, is the so-called detuning and a gradient of this is present across the sample that is induced during growth.

The eigenvectors of the upper and lower polariton states are given by

$$M(k) \cdot \begin{pmatrix} X_i \\ C_i \end{pmatrix} = E_i(k) \cdot \begin{pmatrix} X_i \\ C_i \end{pmatrix}$$

with $|C_i(k)|^2 + |X_i(k)|^2 = 1$ where i=U,L. $C_i(k)$ and $X_i(k)$ are the so called Hopfield coefficients [4], [41] and denote the excitonic or photonic content of the new eigenstates. For the lower polaritons, they are given by:

$$\begin{aligned} C_L(k) &= -\frac{\hbar\Omega}{\sqrt{\hbar^2\Omega^2 + \left(E_L(k) - E_c(k)\right)^2}} \\ X_L(k) &= \frac{E_c(k) - E_L(k)}{\sqrt{\hbar^2\Omega^2 + \left(E_L(k) - E_c(k)\right)^2}} \end{aligned} \qquad (2.12)$$

The detuning, δ, not only changes the form of the upper and lower polariton dispersions, but also affects the excitonic or photonic character of the polaritons. The dispersions of the bare exciton and bare photon modes (dashed red) along with the dispersions of the polariton modes (solid black lines) are shown in Figure 2.5(a)-(c) for three different detunings. The Hopfield coefficients for these three values of detuning are shown in Figure 2.5(d)-(e) where the effect on the character of polaritons can be seen clearly. Although the dispersions of the individual photonic and excitonic modes cross over each other for zero or negative detuning, the polariton modes show a clear anti-crossing.

This anti-crossing, when demonstrated for all different values of detuning, is conclusive evidence of operation in the strong coupling regime. A detailed calculation of the anti-crossing of the upper and lower polariton dispersions for a large range of detuning is shown in Figure 2.6.

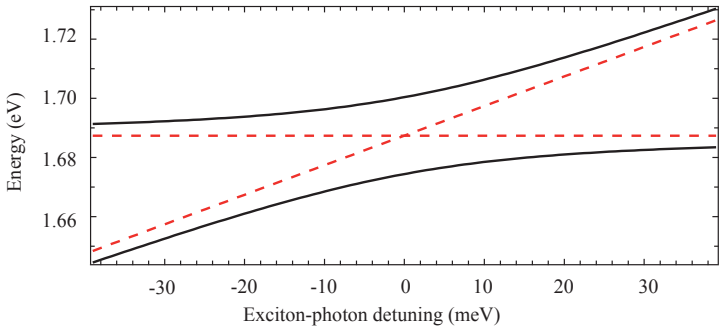

Figure 2.6 Upper and lower polariton energy at $k_{//} = 0$ (solid black lines) for a range of exciton photon detuning. Although the dispersion of the individual exciton and photon cross over each other for zero detuning (dashed lines), the upper and lower polariton dispersions show a clear anti-crossing characteristic of the strong coupling.

It is instructive to consult once more the powerful transfer matrix method and calculate the entire structure of a microcavity with a single quantum well. Introducing the simplified form of the QW transfer matrix using the non-local dielectric response theory [42], [43] allows for the calculation of the full reflectivity spectrum of a strongly coupled microcavity for normal incidence, as shown in Figure 2.7(a), as well as, for the whole range [π/2,–π/2] of incidence angles, as shown in Figure 2.7(b). The reflectivity profile at normal incidence shows a twin peak corresponding to the upper and lower polariton and a clear polariton-like dispersion can be seen in the angle dependent calculated reflectivity.

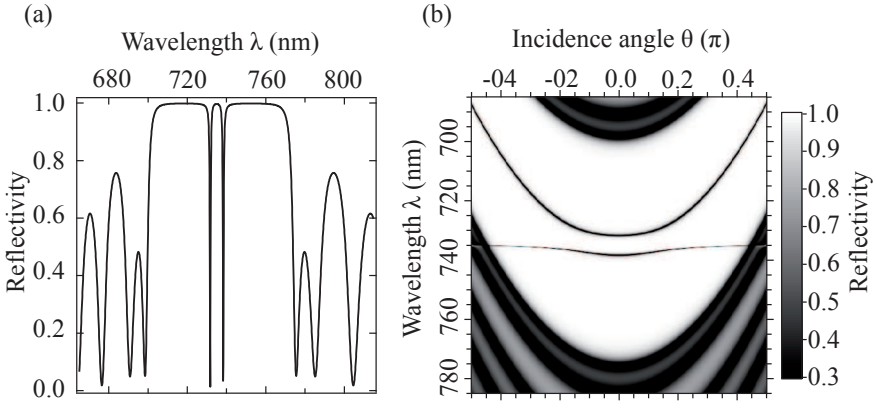

Figure 2.7 Transfer matrix method reflectivity calculations for complete microcavity structure with four quantum wells. The microcavity is identical to the one in Figure 2.3. (a) Reflectivity spectra at normal incidence. (b) Complete angle dependence of the microcavity reflectivity. The polariton dispersion is clearly visible on the stopband of the structure.

2.4 POLARITON CONDENSATES

The extremely low mass of polaritons and the strong binding energy of excitons in II-VI compound microcavities allow for the observation of macroscopically occupied states without loss of the strong coupling. The first experimental evidence by Richard et al. [20] was refuted because the authors had not presented evidence of macroscopic phase coherence in real space. The breakthrough came by the work of the same authors [21], who not only showed the Bose distribution, but also clearly demonstrated evidence of long range order.

2.4.1 Long range order: the normalized first-order correlation function

The appearance of a quantum degenerate macroscopically occupied state leaves its signature also in the coherence properties of the condensate.

According to the criterion of Penrose and Onsager [44], as long as the thermal de Broglie wavelength is much smaller than the system size, condensation should be accompanied by the occurrence of off diagonal long range order. This manifests itself in the form of first order spatial coherence. The definition of the degree of first order spatial coherence is given by [45]:

$$g^{(1)}\left(r_1,t_1;r_2,t_2\right)=\frac{\left\langle E^*\left(r_1,t_1\right)E\left(r_2,t_2\right)\right\rangle}{\sqrt{\left\langle\left|E\left(r_1,t_1\right)\right|^2\right\rangle\left\langle\left|E\left(r_2,t_2\right)\right|^2\right\rangle}} \tag{2.13}$$

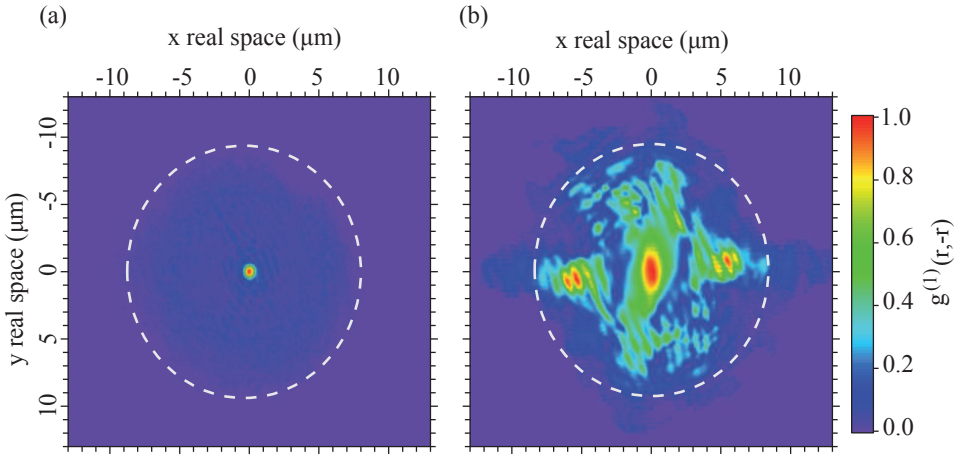

Figure 2.8 Spatial coherence measurement (a) below and (b) above condensation threshold. Below threshold, the coherence is only seen at the autocorrelation point given by the thermal de Broglie wavelength convoluted by the response function of the microscope objective. Above threshold, the coherence is seen all across the excitation spot (dashed white line).

which is a complex quantity. The only straight forward way to evaluate this function is by means of interferometric measurements. As will be shown in the following chapter (Chap. 3, Sects. 3.3.2 -3.4.1) the interferometric measurement that is used for the demonstration of the first order spatial coherence is performed by a modified Michelson interferometer in the mirror-retroreflector configuration that allows the evaluation of the $|g^{(1)}(\mathbf{r}, -\mathbf{r})|$ function. A typical real pace map of the $g^{(1)}$ is provided in Figure 2.8. Below condensation threshold, the coherence extends over a sub-micron region corresponding to the autocorrelation point where light is interfering with itself. Above the condensation threshold, parts of the condensate located at anti-diametrically symmetric positions have a fixed phase relation and, therefore, show high coherence. Of course, other interferometric methods like the Young's double slit experiment can be used to evaluate $g^{(1)}(r_1, t_1; r_2, t_2)$, but it only allows for the evaluation of $g^{(1)}$ for one relative distance r_1 - r_2 at a time.

2.4.2 Gross-Pitaevskii equation (GPE) with pumping and dissipation under CW excitation

One of the most successful theories for the description of exciton-polariton condensates has proven to be the mean field theory. In this framework, the dynamics of the polariton condensates and the non-equilibrium character is described by a generalized Gross-Pitaevskii equation with pumping and dissipation terms coupled to a rate equation for the dynamics of the reservoir to account for the non-resonant pumping. Dissipation is directly related to the limited lifetime of polaritons and its origin can be traced back to their photon component. The existence of a condensate in steady state is, therefore, only possible under continuous replenishing of the condensate from a large reservoir. Here, the excitation laser creates a large incoherent population of excitons that are subsequently scattered to the condensate replenishing the lost particles that have decayed out of the microcavity. Therefore, the steady state is characterized by an equilibrium between the condensate out-going particles and those coming in from the excitonic reservoir. The model and its modifications are described in detail in the later chapters of this book, where it is used to model the experimental findings. Here, only a brief description of the model will be provided with an example of a simulated condensate that occurs in a disorder potential that forces the pinning of a quantized vortex. In this model, the condensates are described by the mean field,

$$\psi(\mathbf{r},t) = \sqrt{n(\mathbf{r},t)}e^{i\varphi(\mathbf{r},t)}$$

which forces them to be fully coherent. As will be shown in the following chapters, the high degree of coherence of the condensates that is seen experimentally

justifies the omission of fluctuation terms. Nevertheless, variations of this model with fluctuations are taken into account where necessary (for the modeling of the properties of coherence). The initial conditions of the condensate wavefunction are set so as to be in a vacuum state with random noise for the phase. Non-resonant pumping fills the excitonic reservoir at a rate of P (**r**) and excitons scatter to the condensate state at a rate of R (n_R (**r**)). The lifetime of the excitons in the reservoir is given by γ_R. The rate equation for the reservoir reads:

$$\frac{\partial n_R(\mathbf{r})}{\partial t} = P(\mathbf{r}) - \gamma_R n_R(\mathbf{r}) - R\left(n_R(\mathbf{r})\right)\left|\psi(\mathbf{r},t)\right|^2 \tag{2.14}$$

The dynamics of the polariton mean field are described by the Gross Pitaevskii equation:

$$\begin{aligned} i\hbar\frac{\partial\psi(\mathbf{r},t)}{\partial t} = \Bigg\{ -\frac{\hbar^2}{2m}\nabla_{\mathbf{r}}^2 + V_d(\mathbf{r}) + \hbar g_R n_R(\mathbf{r}) + \hbar g\left|\psi(\mathbf{r},t)\right|^2 + \\ + \frac{i\hbar}{2}\left[R\left(n_R(\mathbf{r})\right) - \gamma_c\right]\Bigg\}\psi(\mathbf{r},t) \end{aligned} \tag{2.15}$$

where V_d (**r**) is the disorder potential. The interactions between reservoir excitons and condensate polaritons are captured by the term $\hbar g_R$, and polariton-polariton interactions are described by the term $\hbar g$. Polaritons leak out of the condensate at a rate γ_c. This model was introduced by Carusotto and Wouters [46] and was successfully used to describe the finite excitation spotsize effects [47] and the spontaneous formation of rotating vortices in a non-equilibrium polariton condensate [48], among others. As will be seen in subsequent chapters, this model has also been very successful with the description of the appearance and pinning of quantized vortices, as well as, the phenomenon of condensation into multiple spatially overlapping condensates. A simulation using this model for a particular disorder where a condensate with a vortex is found in the steady state can be seen in Figure 2.9 and Figure 2.10. More specifically, Figure 2.9(a) shows the condensate density superposed onto the disorder contour. The vortex is pinned close to a deep disorder minimum at (x,y) = (–5,2.5) μm.

The reservoir density is shown in (b) where the vortex location is also visible from the local density maximum. Figure 2.10(a) shows the phase of the wavefunction and (b) shows the momentum space distribution. The arrows depict the direction of the fluid motion and the arrow length is indicative of the fluid velocity. The outward flow of particles seen by the arrows is due to the blue-shifted effective potential seen by the polaritons that is created by the polariton-polariton and exciton-polariton interactions under the excitation spot.

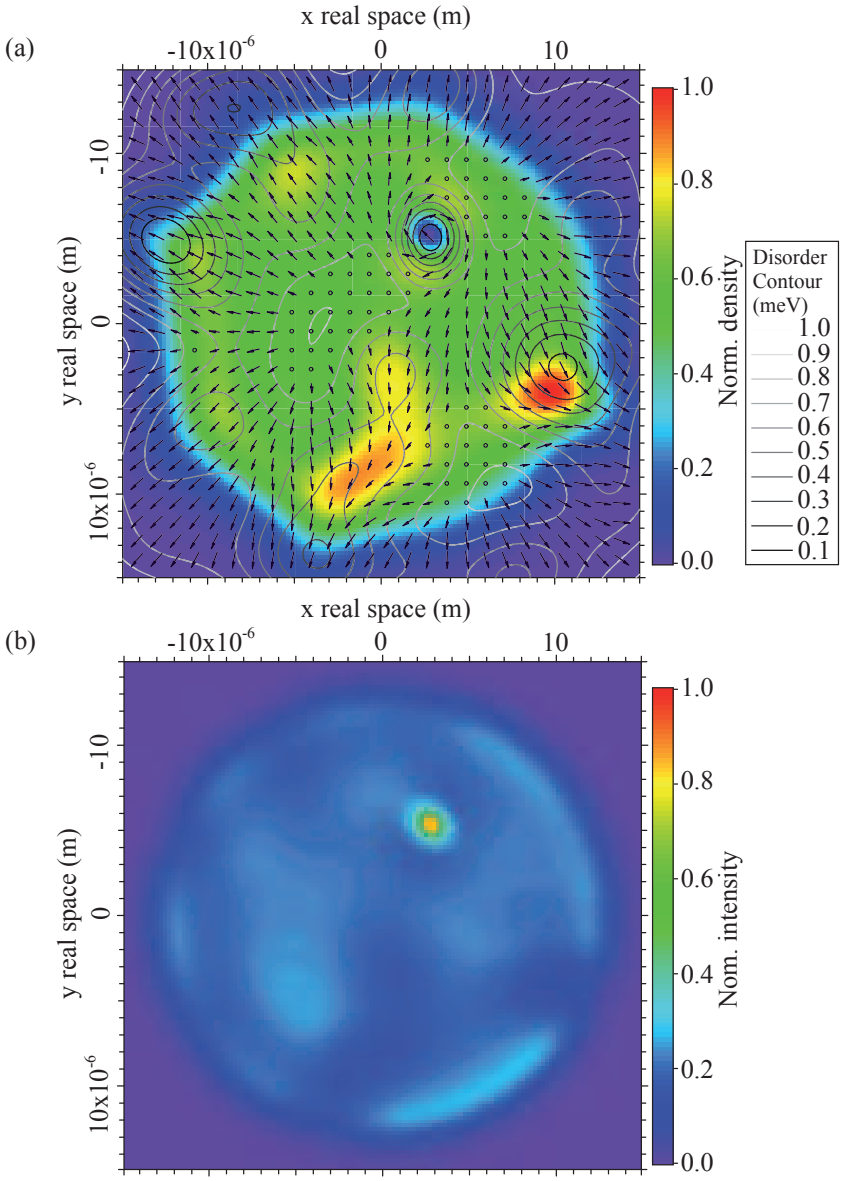

Figure 2.9 (a) Real space polariton density for a disorder potential that forces pinning of a single vortex. The vortex is here pinned at a location that corresponds to a local minimum of the potential at a region that is otherwise a maximum. This "volcano crater" disorder potential shape is one of the disorder structures that are known to force pinning of vortices. The outward flow of particles is due to the blue-shifted effective potential seen by polaritons which are created by polariton-polariton and exciton-polariton interactions under the excitation spot. (b) Excitonic reservoir density. The location of the vortex core is easily distinguishable as it is the only region of the reservoir with higher than average density.

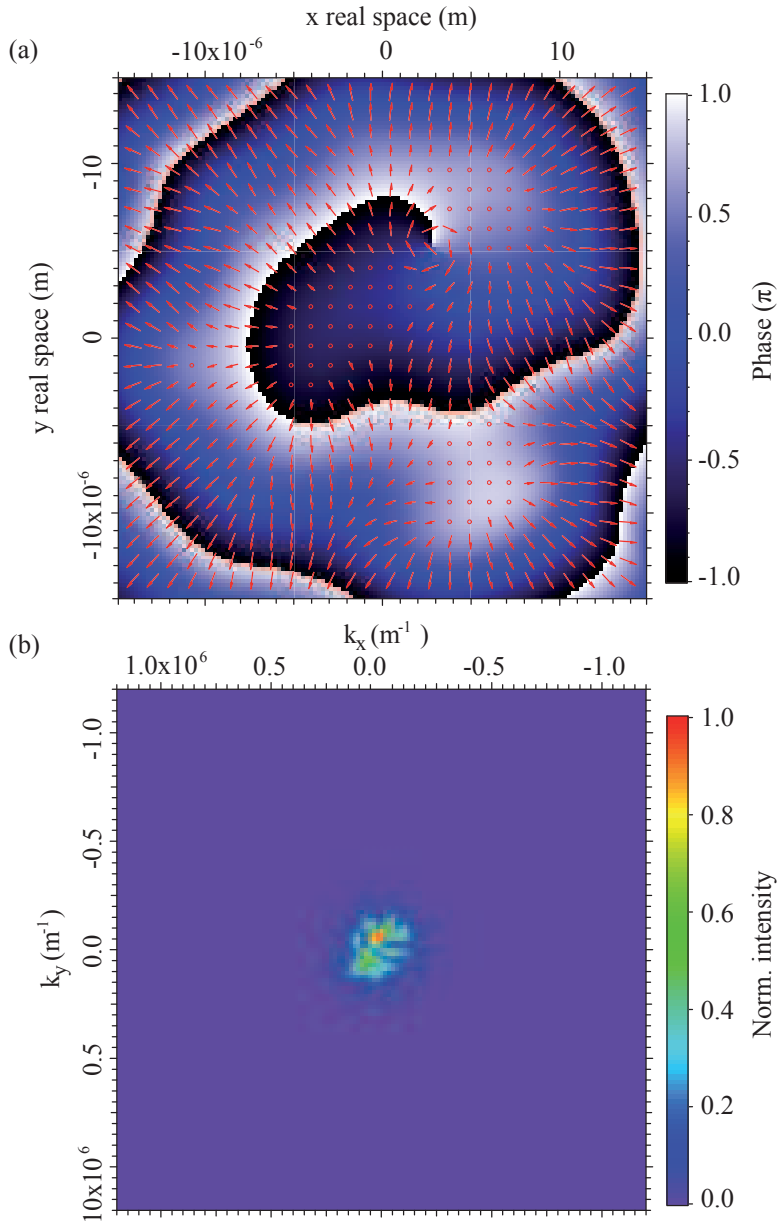

Figure 2.10 (a) Phase of the polariton wavefunction calculated for the same parameters as Figure 2.10. The vortex singularity is clearly visible and the location (x,y) = (–5,2.5) μm. The phase profile shows a spiral structure which comes from both the rotational flow, because of the vortex, and the outward flows, because of the polariton-polariton and exciton-polariton interactions that act as a radial acceleration potential. (b) Momentum space of the polariton fluid. The finite size accounts for the fluid flow described above.

It is worth noting that a single reservoir can hardly capture the complicated dynamics governing the relaxation of excitons from the reservoir region towards the condensate. The dynamics of the condensate population under CW excitation are expected to undergo a smooth transition from an empty condensate to the steady state population. Using realistic parameters for the exciton lifetimes in the single reservoir model produces an oscillatory behavior that does not reproduce the expected dynamics. The oscillations become significantly enhanced for low excitation powers close to condensation threshold. Solving numerically the GPE without spatial degrees of freedom provides a precise overview of the dynamics of the populations in the excitonic reservoir and the condensate. Figure 2.11 shows the population evolution for an excitation power close to the threshold (a) and at three times the threshold (b). The oscillations at the early moments of the condensate formation are clearly visible at both powers, but have striking dimensions at the lowest power.

A simple hand-waving argument for these oscillations is that initially the driving source slowly builds up the reservoir population up to the point that the population is high enough that stimulated scattering to the condensate kicks in and it abruptly empties the reservoir into the condensate. Because of the slow replenishing rate of the reservoir, the fast depletion of the condensate, and the short polariton lifetime, the system goes into a condition that stimulated scattering is inhibited until the reservoir has built up enough population again for the stimulated scattering to manifest. As the condensate is not starting from a completely empty state, the stimulated scattering takes place sooner. The same cycle is done several times with ever decreasing amplitude until a steady state is reached.

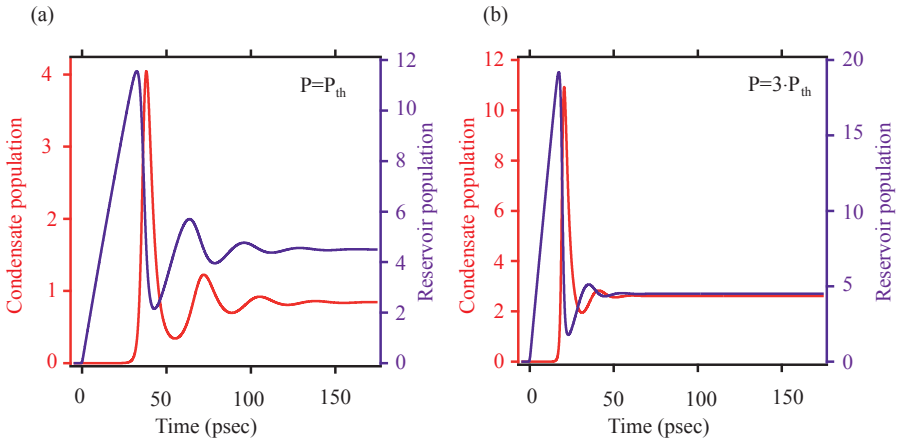

Figure 2.11 Population dynamics for the single reservoir model with realistic exciton reservoir lifetime ($\gamma_R = 0.01\gamma_c$). The results are shown for excitation at threshold power (a) and three times the threshold power (b).

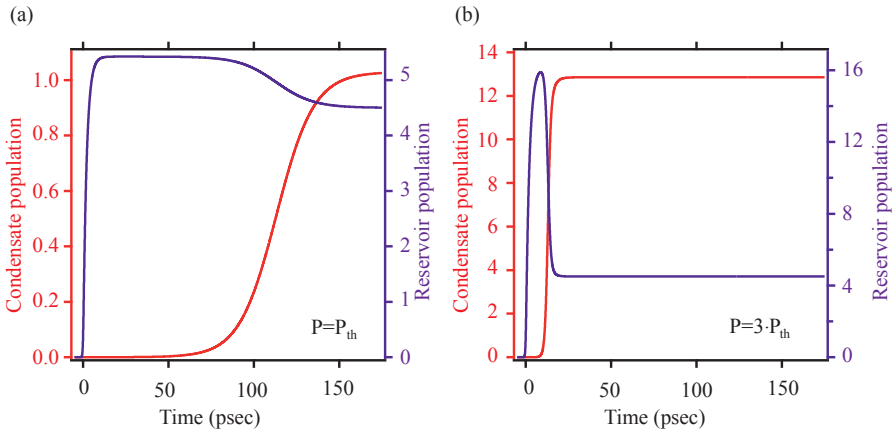

Figure 2.12 Population dynamics for the single reservoir model with non-realistic exciton reservoir lifetime ($\gamma_R = \gamma_c$). The results are shown for excitation at threshold power (a) and three times the threshold power (b).

To overcome this rather annoying issue of oscillatory behavior or 'ringing', the exciton lifetime can be made of the same order or shorter than the polariton lifetime. This change eliminates the ringing and perfectly reproduces the expected temporal behavior as shown in Figure 2.12. For comparison, the same two excitation powers as before are provided. For both excitation powers, the condensate population evolves in a smooth way from empty to the steady state population and, as the excitation power is increased, the dynamics are accelerated: the condensate gets to the steady state within a few picoseconds as opposed to a few hundred for low excitation power.

2.4.3 Modeling polariton condensation under pulsed excitation

Although a single reservoir model perfectly describes the system under CW excitation, allowing for steady state studies, as well as, understanding the dynamics that govern the condensate from its early moments until it reaches the steady state, it is completely inadequate for describing the dynamics under pulsed excitation. In the event of pulsed excitation, the reservoir population would reach its maximum within the duration of the pulse. That would trigger the stimulation to the condensate state which would completely deplete the reservoir forcing the system to finally decay at the rate imposed by the polariton lifetime, thus making the condensate extremely short lived. In order to overcome this issue and to capture the dynamics of polariton condensation under pulsed excitation, a double reservoir model was introduced by Wouters in the work of Nardin et al. [49]. A simplified version of this model is presented here.

The main element of this model is the separation of the excitonic reservoir in two sub-sets: one reservoir in which excitons satisfy energy and momentum conservation to scatter into the condensate (active) and one reservoir that the excitons cannot scatter to the condensate directly (inactive). The incoherent pump is here replenishing the inactive reservoir at a rate $P(\mathbf{r},t)$ and part of those excitons transfer to the active reservoir at a rate R_{IA}. Active excitons can then scatter directly to the condensate at a rate R_R and back to the inactive reservoir at a rate R_{AI}. Excitons in both the active and inactive reservoirs are long lived with lifetimes given by γ_A and γ_I. The system of three equations (two reservoir rate equations and the GPE) is provided here.

The inactive reservoir rate equation is

$$\frac{\partial n_I(\mathbf{r},t)}{\partial t} = -\left(R_{IA}+\gamma_I\right)n_I(\mathbf{r},t) + R_{AI}n_A(\mathbf{r},t) + P(\mathbf{r},t) \tag{2.16}$$

while the active reservoir rate equation is given by

$$\frac{\partial n_A(\mathbf{r},t)}{\partial t} = -\left(\gamma_A + \alpha R_R\left|\psi(\mathbf{r},t)\right|^2 + R_{AI}\right)n_A(\mathbf{r},t) + R_{IA}n_I(\mathbf{r},t) \tag{2.17}$$

Note that excitons leave the reservoir via three channels: either they can decay due to the limited lifetime, scatter back to the incoherent reservoir, or scatter to the condensate. The term α is a term describing the depletion of the excitonic reservoir due to stimulated scattering in the condensate.

$$i\hbar\frac{\partial\psi(\mathbf{r},t)}{\partial t} = \left\{-\frac{\hbar^2\nabla^2}{2m} + g\left|\psi(\mathbf{r},t)\right|^2 + V(\mathbf{r}) + \hbar g_R\left[n_A(\mathbf{r},t)+n_I(\mathbf{r},t)\right] + \right.$$
$$\left. + \frac{i}{2}\left[\gamma_c - R_R n_A(\mathbf{r},t)\right]\right\}\psi(\mathbf{r},t) \tag{2.18}$$

Using this double reservoir concept allows the stimulation of particles to the condensate state to be regulated while preventing the rapid depletion of the excitons. This phenomenon in turn permits the undisrupted feeding of the condensate over several hundreds of picoseconds closely reproducing the experimentally observed behavior. Figure 2.13 shows the temporal evolution for the populations in the condensate along with the active and inactive reservoirs for two excitation powers. At threshold, a slow response of the system is seen at around 80 psec, while for higher powers the condensate population dynamics are accelerated towards the excitation pulse arrival. Several variations of this model have been used in dynamical experiments as will be seen in the following chapters.

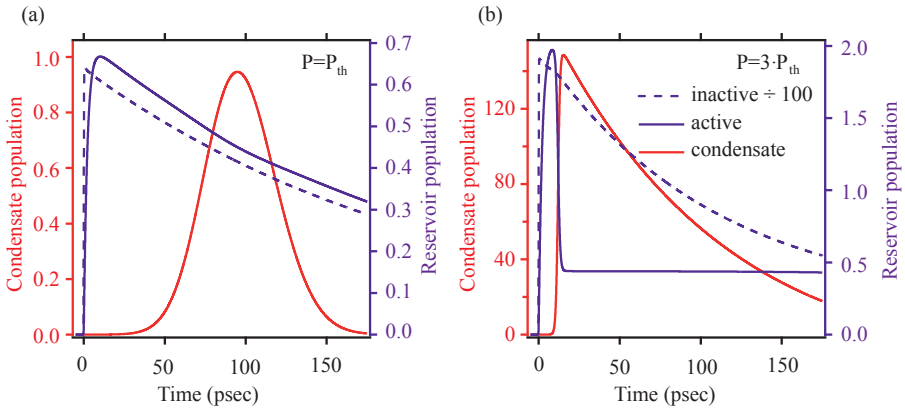

Figure 2.13 Dynamics of populations for the double reservoir model. The two panels correspond to two excitation powers: threshold power (a) and three times the threshold power (b). The inactive reservoir population in both panels is the dashed line and is divided by a factor of 100 to fit on the same scale as the active reservoir population. The results are reproducing very closely the temporal behavior of polariton condensation under pulsed excitation.